

# The effects of rheological decoupling on slab deformation in the Earth's upper mantle

ADELA ANDROVIČOVÁ<sup>1</sup>, HANA ČÍŽKOVÁ<sup>1</sup> AND ARIE VAN DEN BERG<sup>2</sup>

- 1 Faculty of Mathematics and Physics, Charles University in Prague, V Holešovičkách 2, 180 00 Praha 8, Czech Republic (Hana.Cizkova@mff.cuni.cz)
- 2 Institute of Earth Sciences, Utrecht University, Budapestlaan 4, 3584 CD Utrecht, The Netherlands

*Received: August 22, 2012; Revised: December 5, 2012; Accepted: December 10, 2012*

---

## ABSTRACT

*Processes within subduction zones have a major influence on the plate dynamics and mantle convection. Subduction is controlled by a combination of many parameters and there is no simple global relationship between the resulting slab geometry and deformation and any specific subduction parameter. In the present work we perform a parametric study of slab dynamics in a two-dimensional model with composite rheology including diffusion creep, dislocation creep and stress limiter or Peierls creep. The mechanical decoupling of the subducting and overriding plates is facilitated by a low viscosity crust. We are particularly interested in the effect of the contact of subducting and overriding plates on the plate geometry in the upper mantle. We also study the influence of the surface boundary condition and of the rheological description (yield stress of stress-limiting rheology, additional viscosity contrast at 660-km discontinuity). Our results demonstrate that the slab morphology and deformation in the upper mantle and the transition zone is sensitive not only to the slab strength, but also to the decoupling mechanism at the contact of the subducting and overriding plates. Weak crust with a viscosity of  $10^{20}$  Pa s effectively decouples the subducting and overriding plates and produces reasonable slab morphologies. The geometry of the slab in the upper mantle is strongly influenced by the initial geometry of the contact between the subducting and overriding plates. Further, a step-wise viscosity increase by about an order of magnitude at 660 km depth is necessary to limit the plate velocities to a reasonable value around 5 cm/yr.*

Keywords: subduction, slab deformation, rheology

## 1. INTRODUCTION

Seismic tomography is able to map the seismic velocity anomalies associated with the subducted slabs deep into the mantle (*van der Meer et al., 2010*). The advances in tomographic imaging have been accompanied by the development of the numerical modelling of the subduction process. More and more sophisticated models of the slab deformation process address physical effects including complex rheologies or phase

changes and related material properties as well as more technical aspects including the effects of boundary condition or 2D vs. 3D geometry (e.g. *Billen, 2010; Jadamec and Billen, 2010; Quinquis et al., 2011; Lee and King, 2011; Quinteros and Sobolev, 2012; Jacobs and van den Berg, 2011; Maierova et al., 2012; Rolf and Tackley, 2011; Chertova et al., 2012*). Despite unequivocal advances, there are still a large number of issues that have not been resolved. Among them the questions related to the mechanisms that facilitate the subduction process on the contact of the subducting and overriding plates are still waiting for more elaborate analysis.

The processes occurring at the contact of the plates are not well understood, although it is generally thought that rheological weakening due to hydration of crustal material is a key factor. Water present in the crust (*van Avendonk et al., 2010, 2011*) may reduce the viscosity and thus enable sliding of one plate over another resulting in one-sided subduction pattern (*Hirth and Kohlstedt, 2003*). In order to generate the tectonic plates within the mantle convection models, shear localization was recognized as a crucial ingredient (*Zhong et al., 1998; Bercovici, 1998; Bercovici et al., 2000; Bercovici et al., 2001; Regenauer-Lieb and Yuen, 2003; Auth et al., 2003*). A narrow zone where the deformation occurs has until recently (e.g. *Sizova et al., 2010; Gerya and Meilick, 2011; Duretz et al., 2011*) remained beyond the reach of the resolution of the numerical models. Thus some approximations had to be used. *Gurnis and Hager (1988)* or *King and Hager (1994)* prescribed a low viscosity weak zone in the uppermost part of the downgoing material in order to get a reasonable morphology of the downwelling. Such weak zone was a priori defined static feature and did not reflect the time evolution of the system – the subducting plate was kept at the same position. The attempts to obtain a realistic plate-like behavior in the convection models proceeded further by considering a strongly power-law rheology (*Schmeling, 1989; King and Hager, 1990; van den Berg et al., 1991*) or dynamic feedback between temperature dependent viscosity and viscous heating (*Balachandar et al., 1995ab; Larsen et al., 1995, 1996; Bercovici, 1996; Bercovici, 1998*). The concept of weakening at the contact of the plates was further elaborated by introducing more sophisticated stress dependent self-lubricating rheologies (e.g. *Trompert and Hansen, 1998; Moresi and Solomatov, 1998; Tackley, 1998, 2000abcd; Richards et al., 2001; Auth et al., 2003; Bercovici, 2003; Bercovici and Ricard, 2003; Ricard and Bercovici, 2003; Stein et al., 2004; van Heck and Tackley, 2008; Stein and Hansen, 2008*). This approach enabled the lateral movement of the downwellings - the weak contact zone developed at the positions of large stress accumulation. Even in these models, however, the subduction was two sided rather than one sided as observed on the Earth (*Gerya et al., 2008*). Alternatively, low friction (or even free-slip) static faults or narrow low-viscosity shear zones have been prescribed at the contact of two strong plates (*Zhong and Gurnis, 1986; Zhong et al., 1998; Kincaid and Sacks, 1997; Billen et al., 2003; van Hunen et al., 2000; Čížková et al., 2002; Billen and Hirth, 2005, 2007; van Hunen and Allen, 2011*). In these models one plate subducts underneath the other one and one-sided subduction is obtained. The geometry of the fixed predefined fault or shear zone that is not updated following the deformation of the plates however inevitably affects the resulting geometry and the deformation of the plate. That could be partly avoided by using a fault or narrow weak subduction channel whose position is updated every time step (*Zhong and Gurnis, 1995a,b; Han and Gurnis, 1999; Kukačka and Matyska, 2004; Sobolev and Babeyko, 2005; Quinteros et al., 2010*). Alternatively, prescribing a narrow low viscosity crustal

layer on top of the whole subducting plate (Běhounková and Čížková, 2008; Quinquis et al., 2011; Chertova et al., 2012) may also facilitate decoupling without much affecting the geometry of the contact. The geometry of the contact is only specified at the beginning and then evolves with the two plates and depends primarily on their rheological properties and on the rheology of the crust.

Here we follow the same strategy - we prescribe a thin, low viscosity layer representing the crust on top of the subducting plate and study the shallow deformation of the slab as a function of the parameters of this contact. We present a group of subduction models that differ in i) surface boundary condition, ii) crustal rheological description, iii) initial crustal geometry and iv) stress limiter parametrization determining slab rheology. We will demonstrate to what extent these parameters influence the slab dynamics and the resulting slab geometry in the upper mantle and the transition zone.

## 2. MODEL DESCRIPTION

The subduction of the lithospheric plates is driven by the buoyancy forces associated with the thermal and compositional anomalies in the mantle. The dynamic evolution of the plates is described by a set of equations including continuity, momentum and thermal equations. Here we use the incompressible extended Boussinesq approximation of the governing equations (Ita and King, 1994) without internal heating:

$$\nabla \cdot \mathbf{u} = 0, \quad (1)$$

$$\nabla \cdot \boldsymbol{\tau} + \rho \mathbf{g} = 0, \quad (2)$$

$$\frac{\partial T}{\partial t} = -\mathbf{u} \cdot \nabla T + \nabla \cdot (\kappa \nabla T) - \frac{w \alpha T g}{c_p} + \frac{1}{\rho_0 c_p} \boldsymbol{\sigma} : \nabla \mathbf{u} + \sum_k \frac{\gamma_k \delta \rho_k T}{\rho_0^2 c_p} \frac{d\Gamma_k}{dt}. \quad (3)$$

Terms on the right hand side of thermal equation (3) represent heat advection, conduction, adiabatic heating, viscous heating and latent heat associated with the major mantle phase transitions respectively.  $\Gamma_k$  is a phase function characterising the  $k$ -th phase transition (van Hunen et al., 2001). For the meaning of the symbols see Table 1. We use following constitutive equation:

$$\boldsymbol{\tau} = -\Delta P \mathbf{I} + \eta_{eff} \dot{\boldsymbol{\epsilon}}, \quad (4)$$

where  $\eta_{eff}$  is effective viscosity, combining the viscosities of individual creep mechanisms (van den Berg et al., 1993):

$$\eta_{eff} = \left( \frac{1}{\eta_{diff}} + \frac{1}{\eta_{disl}} + \frac{1}{\eta_L} \right)^{-1}. \quad (5)$$

Viscosities on the right hand side of Eq. (5) represent linear diffusion creep, power-law dislocation creep and a power-law stress limiter (van Hunen et al., 2002):

$$\eta_{diff} = A_{diff}^{-1} \exp \left( \frac{E_{diff}^* + PV_{diff}^*}{RT} \right), \quad (6)$$

**Table 1.** List of the used parameters, prefactors and powerlaw exponents.

Symbol	Meaning	Value used	Dimension
$A_{diff}$	pre-exponential parameter of diffusion creep (mantle) <sup>a</sup>	$1.92 \times 10^{-10}$	$\text{Pa}^{-1}\text{s}^{-1}$
$A_{disl}$	pre-exponential parameter of dislocation creep (mantle) <sup>a</sup>	$2.42 \times 10^{-15}$	$\text{Pa}^{-n}\text{s}^{-1}$
$A_p$	pre-exponential parameter of Peierls creep (mantle) <sup>b</sup>	$5.7 \times 10^{11}$	$\text{s}^{-1}$
$c_p$	specific heat	1250	$\text{J kg}^{-1}\text{K}^{-1}$
$\kappa$	thermal diffusivity	$10^{-6}$	$\text{W m}^2\text{J}^{-1}$
$g$	gravitational acceleration	9.8	$\text{m s}^{-2}$
$E_{diff}^*$	activation energy of diffusion creep (mantle) <sup>c</sup>	$3 \times 10^5$	$\text{J mol}^{-1}$
$E_{disl}^*$	activation energy of dislocation creep (mantle) <sup>c</sup>	$5.4 \times 10^5$	$\text{J mol}^{-1}$
$V_{diff}^*$	activation volume of diffusion creep (mantle) <sup>a</sup>	$4.5 \times 10^{-6}$	$\text{m}^3\text{mol}^{-1}$
$V_{disl}^*$	activation volume of dislocation creep (mantle) <sup>a</sup>	$14 \times 10^{-6}$	$\text{m}^3\text{mol}^{-1}$
$n$	viscosity stress exponent <sup>c</sup>	3.5	---
$n_L$	yield stress exponent	5	---
$R$	gas constant	8.3143	$\text{J K}^{-1}\text{mol}^{-1}$
$\gamma$	Peierls creep constant <sup>b</sup>	0.1	---
$\sigma_p$	Peierls stress <sup>b</sup>	$3-8.5 \times 10^9$	Pa
$g_p$	Peierls creep parameter <sup>b</sup>	31	---
$q$	stress dependence for Peierls creep <sup>b</sup>	2	---
$T$	temperature	---	K
$T_m$	melting temperature	---	K
$T_s$	surface temperature	273	K
$p$	total pressure	---	Pa
$P$	hydrostatic pressure	---	Pa
$\Delta P$	dynamic pressure	---	Pa
$\Delta T$	temperature contrast across model domain	2300	K
$t$	time	---	s

$$\eta_{disl} = A_{disl}^{-1/n} \dot{\epsilon}^{(1-n)/n} \exp\left(\frac{E_{disl}^* + PV_{disl}^*}{nRT}\right), \quad (7)$$

$$\eta_L = \sigma_L \dot{\epsilon}_L^{-1/n_L} \dot{\epsilon}^{1/n_L - 1}. \quad (8)$$

The activation parameters, prefactors and powerlaw exponents are given in Table 1. The effect of the yield stress  $\sigma_L$  of the stress limiting rheology is tested in the range 0.1 – 1 GPa. The power-law stress limiter may be used in subduction simulations (van Hunen *et al.*, 2002; Čížková *et al.*, 2002) as an effective approximation of low temperature plasticity (Kameyama *et al.*, 1999). In some models here we also test the effect of the Peierls creep deformation process. In these models the viscosity of the stress limiter  $\eta_L$  in eq.(8) will be replaced by the Peierls creep viscosity (Kameyama *et al.*, 1999):

**Table 1.** Continuation.

Symbol	Meaning	Value used	Dimension
$\mathbf{u}$	velocity $\mathbf{u} = (v, w)^T$	---	$\text{m s}^{-1}$
$\alpha$	thermal expansion coefficient	$3 \times 10^{-5}$	$\text{K}^{-1}$
$\Gamma_k$	phase functions for all $k$ mantle phase transitions	---	---
$\gamma_{400}$	Clapeyron slope 400 km phase transition <sup>d</sup>	3	$\text{MPa K}^{-1}$
$\gamma_{670}$	Clapeyron slope 670 km phase transition <sup>d</sup>	-2.5	$\text{MPa K}^{-1}$
$\delta\rho_{400}$	density difference across the 400 km phase transition <sup>e</sup>	273	$\text{kg m}^{-3}$
$\delta\rho_{670}$	density difference across the 670 km phase transition <sup>e</sup>	342	$\text{kg m}^{-3}$
$\dot{\epsilon}$	$\dot{\epsilon}_{ij} = \partial_j u_i + \partial_i u_j =$ strain rate tensor	---	$\text{s}^{-1}$
$\dot{\epsilon}$	2 <sup>nd</sup> invariant of the strain rate	---	$\text{s}^{-1}$
$\dot{\epsilon}_L$	reference strain rate in yield strength determination	$10^{-14}$	$\text{s}^{-1}$
$\eta$	viscosity	---	$\text{Pa s}$
$\eta_0$	reference viscosity	$10^{21}$	$\text{Pa s}$
$\eta_c$	viscosity of the crust	$10^{19}-10^{21}$	$\text{Pa s}$
$\rho_0$	reference density corresponding to temperature $T_s$	3416	$\text{kg m}^{-3}$
$\sigma_L$	yield stress	---	$\text{Pa}$
$\sigma$	deviatoric stress tensor	---	$\text{Pa}$
$\tau$	total stress tensor $\tau_{ij} = -\Delta P \delta_{ij} + \sigma_{ij}$	---	$\text{Pa}$
$\sigma_{II}$	2 <sup>nd</sup> invariant of the deviatoric stress tensor $\sigma_{ij}$	---	$\text{Pa}$
$\tau$	2 <sup>nd</sup> invariant of the total stress tensor $\tau_{ij}$	---	$\text{Pa}$

<sup>a</sup> Modified from *Karato and Wu (1993)* to meet the constraints from postglacial rebound models, *van Hunen et al. (2004)*

<sup>b</sup> *Kameyama et al. (1999)*

<sup>c</sup> *Karato and Wu (1993)*

<sup>d</sup> *Bina and Helffrich (1994)*

<sup>e</sup> *Steinbach and Yuen (1995)*

$$\eta_P = A_P^{-(1/S(T))} \dot{\epsilon}^{(1/S(T))-1} \gamma \sigma_P \exp \left( g_P \frac{T_m(P)}{TS(T)} (1 - \gamma)^q \right), \quad (9)$$

where

$$S(T) = \frac{g_P T_m(P)}{T} (1 - \gamma)^{q-1} q \gamma \quad (10)$$

and  $T_m(P)$  is melting temperature (*McNamara et al., 2001*) parameterised in terms of the depth  $z$  as:

$$T_m = 2100 + 1.4848z - 5 \times 10^{-4} z^2 \quad (11)$$

in the upper mantle and

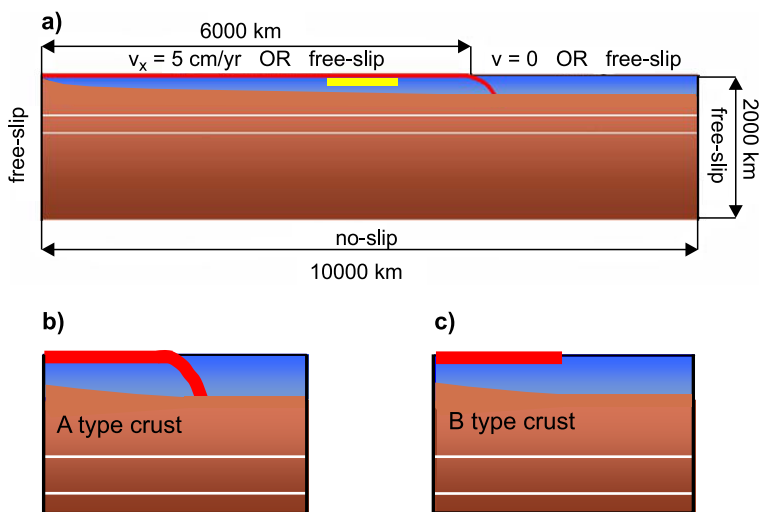
$$T_m = 2916 + 1.25z - 165 \times 10^{-4}z^2 \quad (12)$$

in the lower mantle. In these runs the effective viscosity is

$$\eta_{eff} = \left( \frac{1}{\eta_{diff}} + \frac{1}{\eta_{dist}} + \frac{1}{\eta_P} \right)^{-1} \quad (13)$$

Density variations are linearly proportional to the thermal variations, thermal expansion coefficient is assumed to be constant. For the meaning of the symbols and parameter values see Table 1. We solve the system by finite element methods using the package SEPRAN (Segal and Praagman, 2005).

We use a 2D Cartesian model. Our model domain represents the upper 2000 km of the mantle and it is 10000 km wide (Fig. 1a). Around the depths of 410 km and 660 km major mantle phase transitions are prescribed using the phase function parameterization (e.g. van Hunen et al. 2001) with the parameters given in Table 1. The bottom and the side boundaries of the model domain are free-slip impermeable. On the top we prescribe either velocity or free-slip. In the model cases with the kinematic boundary condition a constant horizontal velocity of 5 cm/yr is prescribed on the subducting plate while the overriding plate is characterized by a no slip boundary condition. At the top and bottom boundaries constant temperatures are prescribed (273 K and 2573 K respectively) and zero heat flux on the sides. The temperature initial condition is obtained as follows. In the subducting



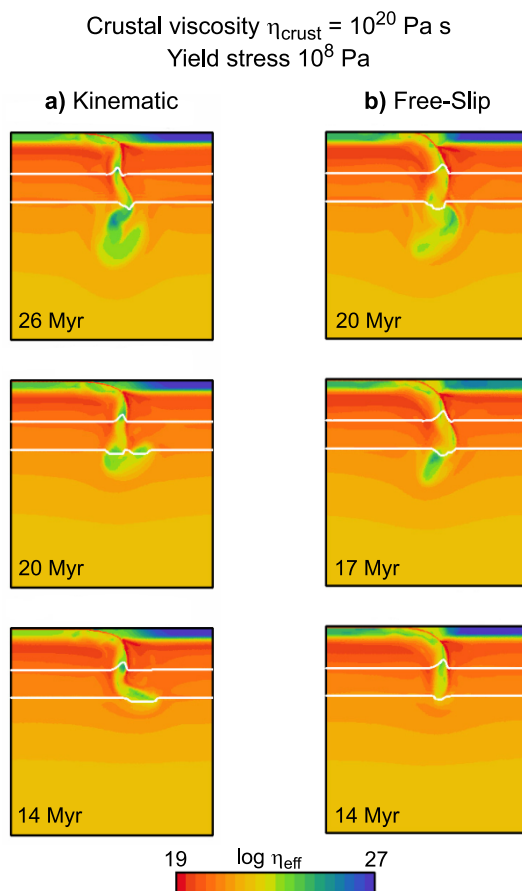
**Fig. 1.** Model set-up and the boundary conditions. **a)** Sketch of model domain. Subducting and overriding plates are depicted in blue, red layer on the top of the subducting plate is crust. White lines are for the phase boundaries at 410 km and 660 km. Yellow rectangle marks the area used to calculate average plate velocity. **b)** Close up of the part of the model domain around the contact of the plates with crust initially decoupling subducting and overriding plate (type A models). **c)** Close up of the part of the model domain around the contact of the plates in the models where the crust initially does not separate the subducting and overriding plates (type B models).

plate a half space model is used with a spreading velocity of 5 cm/yr. The plate is 6000 km long and its age at the trench is 120 Myr (plate is about 120 km thick). The overriding plate has a constant thickness and the temperature distribution corresponding to 120 Myr old lithosphere. Below the plates the temperature follows an adiabatic profile with a potential temperature of 1573 K. The ridge push due to the increasing thickness of the ageing oceanic plate is sufficient for setting of subduction from a free-slip initial configuration where a low viscosity layer separates the subducting and overriding plates (see Fig. 1b). Numerical resolution is strongly irregular. Finest resolution is in the area of the contact between the subducting and overriding plates (1.4 km), larger elements (15 km) are at the bottom of the transition zone and extremely coarse grid is used at the bottom corners of the domain (150 km).

The decoupling of the subducting and overriding plates is facilitated by the presence of a low viscosity layer of 10 km thickness representing the crust. This weak layer with constant viscosity  $\eta_c$  is prescribed along the top of the subducting plate from the spreading ridge positioned in the upper left corner of the model domain to the trench originally placed 6000 km from the ridge. No density anomaly is associated with this crust-like layer - its only purpose is mechanical decoupling of the plates. The position of the crust is tracked using particle tracers and it is moving with the subducting plate. At the depth of 200 km it is replaced by mantle material for numerical convenience. As the main focus of this paper is on the effect of the shallow decoupling of the plates, we test here two initial geometries of the crust corresponding to two model types labeled A and B in the following text. In models of type A we follow the strategy of *Běhouňková and Čížková (2008)* and we initially prescribe the weak material along the contact of the subducting and overriding plates (see Fig. 1b). Crust separating the plates initially follows an arc with a radius of 800 km. In the models of type B the crust is initially only prescribed along the surface of the subducting plate (Fig. 1c). In this second group of models a kinematic boundary condition is prescribed at the top and due to the discontinuity in the prescribed horizontal velocity (cf. Fig. 1a) combined with the viscosity contrast between the crust and overriding plate, a shear zone develops below the end of the subducting plate. The nonlinear rheology then ensures the weakening within this shear zone. The geometry of the contact is thus not prescribed a priori - instead it develops reflecting the rheological description of the plates.

### 3. RESULTS

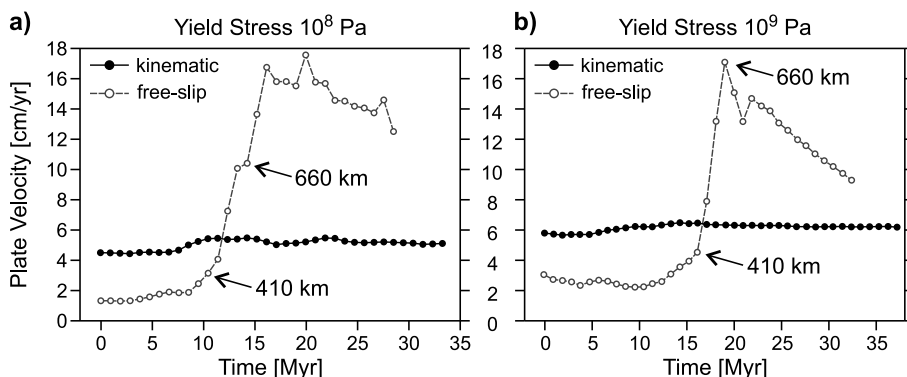
First we present results from model group A, with a weak crustal arc between the subducting and overriding plates. In all these models the power-law stress limiter (Eq. (8)) was applied. The relative importance of the individual deformation mechanisms (diffusion creep, dislocation creep, stress limiter) differs in different parts of the model domain. Except of the slab and its neighbourhood, mantle mostly deforms via diffusion creep. The zone around the subducting slab with relatively high strain-rates deforms predominantly via dislocation creep and the coldest inner parts of the slab deform via stress-limiting mechanism. Fig. 2 illustrates the effects of the surface boundary condition. Here the time evolution of viscosity is shown for models with a prescribed constant surface velocity of



**Fig. 2.** Slab evolution in the modes with crustal viscosity of  $10^{20}$  Pa s and yield stress of 0.1 GPa. **a)** Model with kinematic boundary condition at the subducting plate. **b)** Model with free-slip on the top of the subducting plate. Part of the model domain 2000 km wide and 2000 km deep centered around the trench is shown. White lines mark the positions of the 410 km and 660 km phase transitions.

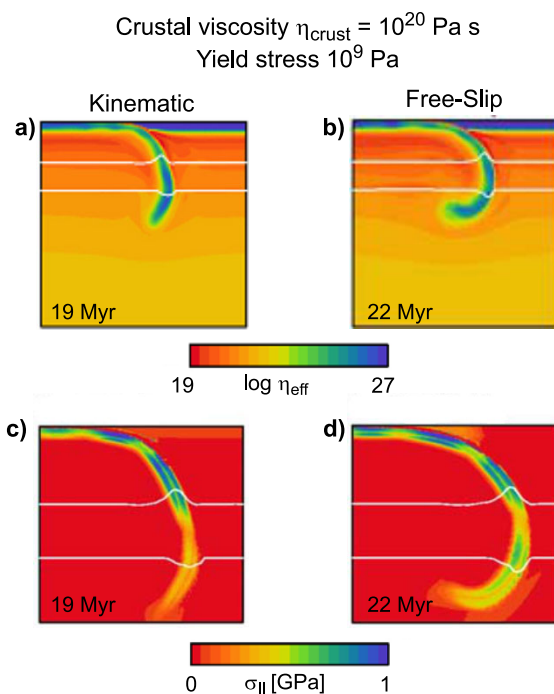
5 cm/yr (column a) and a free-slip surface model (column b). In both models the same yield stress of 0.1 GPa and the same crustal viscosity of  $10^{20}$  Pa s were used. For each model three snapshots were chosen that show the situation after the moments when the slab arrives at the bottom of the transition zone, penetrates to the lower mantle and finally reaches the depth of about 1000 km. In both models we clearly observe the effects of the stress dependent rheology - the viscosity is relatively low where the slab is bending or compressed by the combined effects of the phase transitions (see e.g. the middle panel of the left column). The details of the slab morphology are different as a consequence of differences in the stress fields within the slabs. The stresses generated in the kinematic

case by a boundary condition affect the viscosities through the non-linear rheology and result in different morphology of the subducting plate and different geometry of the contact between the subducting and overriding plates. Despite these differences, we can generally conclude that the basic features are consistent for both types of boundary conditions - the slab is deformed by the resistance of the 660 km phase transition (see middle panels in both columns) but finally penetrates to the lower mantle showing strong buckling. However, what significantly differs is plate velocity. After 14 Myr evolution from an initial state the kinematically driven slab already rests at 660 km boundary while in the free-slip run the slab tip only just reaches that depth at the same time. Later however the free-slip slab becomes faster than the kinematically driven slab and reaches the mid-mantle faster. This is more clearly demonstrated in Fig. 3a, where the plate velocities are shown as a function of time for both models. Plate velocity is defined as an average velocity calculated over the window 1000 km wide and 30 km deep located in the stiff lithospheric plate below the crust 1000 km left from the trench (marked by a rectangle in the upper part of subducting plate in Fig. 1a). While in the kinematic model (full circles) the plate velocity remains close to the prescribed value of 5 cm/yr (small variations are due to the fact that the weak crust does not perfectly transfer the prescribed velocity to the stiff plate below it (Běhounková and Čížková, 2008)), in the free-slip model (open circles) the plate velocity reacts to the buoyancy forces exerted by the phase transitions. The plate, initially very slow because of the small negative buoyancy of the subducted slab accelerates strongly as the slab tip crosses the 410 km phase transition (Čížková et al., 2007). Then it shows a small decrease of velocity as it is impeded by the effect of the 660 km interface. We should also note here that even though the slab slows down after the phase change at 660 km depth it is still keeping a rather high velocity of more than 10 cm/yr. As will be shown below, that could be reduced either by assuming a higher viscosity lower mantle or a stiffer crust.



**Fig. 3.** Plate velocity as a function of time for the models with crustal viscosity of  $10^{20}$  Pa s. Plate velocity is defined as an average velocity calculated over the window 1000 km wide and 30 km deep located in the stiff lithospheric plate below the crust 1000 km left from the trench. **a)** Yield stress 0.1 GPa, kinematic boundary condition (full circles) vs. free-slip (open circles), **b)** yield stress 1 GPa, kinematic boundary condition (full circles) vs. free-slip (open circles).

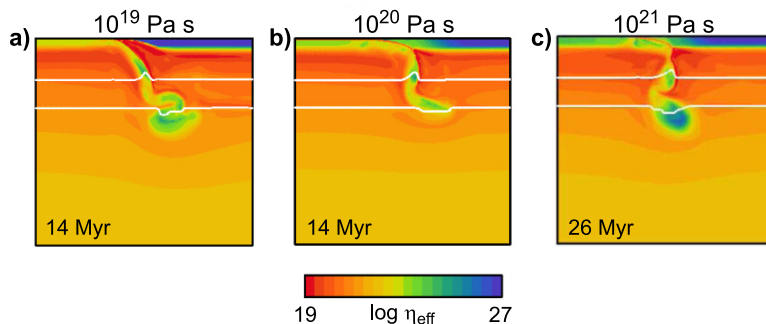
Fig. 4 shows the similar comparison but now for a higher yield stress of 1 GPa. Crustal viscosity is again  $10^{20}$  Pa s. The left column is for a kinematic boundary condition, while the right one is for a free-slip surface. Figs 4a and 4b show the viscosity distributions at the moments when the model slabs reach the depth of about 1000 km, Figs 4c and 4d show zoom-in plots of the corresponding second invariant of the deviatoric stress. In both cases the slab penetrates the 660 km interface and reaches the lower mantle. Both models also produce similar stress and viscosity pattern in the upper mantle. The main difference is the geometry - the free-slip slab experiences significant backwards deflection while the kinematically driven one does not. This is due to the fact that in the free-slip model the slab descent through the transition zone is very fast (cf. the dashed curve in Fig. 3b) due to the accelerating effect of the 410 exothermic phase transition. It is thus keeping the initial curvature it obtained when moving along the predefined subduction slab channel (initial low viscosity crustal arc). The slowly moving kinematically driven slab on the other hand has



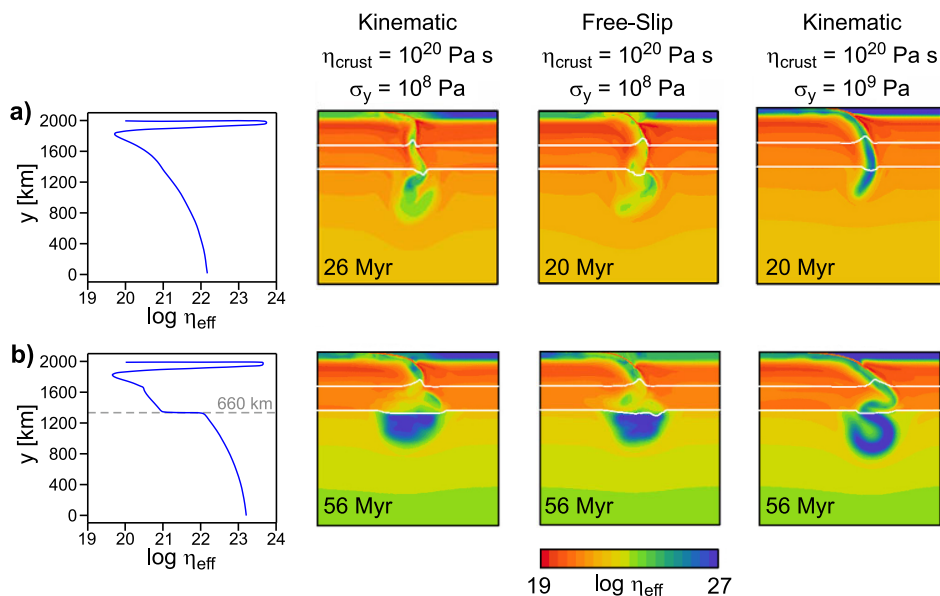
**Fig. 4.** Slab morphology in the models with yield stress 1 GPa and crustal viscosity  $10^{20}$  Pa s. **a)** Effective viscosity at a time snapshot taken after 19 Myr evolution from the initial state in a kinematic boundary condition model. Part of the model domain 2000 km wide and 2000 km deep centered around the trench is shown. White lines mark the positions of the 410 km and 660 km phase transitions. **b)** The same as a), but for a free-slip model after 22 Myr evolution from the initial state. **c)** Second invariant of the deviatoric stress in the same model and snapshot as a). A detail of the model domain, 1000 km deep and 1000 km wide is now shown. **d)** Second invariant of the deviatoric stress in the same model and snapshot as b). A detail of the model domain, 1000 km deep and 1000 km wide is now shown.

enough time to unbend and thus reaches the lower mantle almost vertically. The different slab morphology in the lower mantle is also reflected in the stress pattern – the free-slip slab shows a stress pattern typical for bending in the upper part of the lower mantle (two layers of the relatively high second invariant of stress corresponding to tension and compression divided by a layer of a very low stress (Čížková et al., 2007)) as the deflected part is pushed down. A similar pattern, but with significantly lower amplitude is also observed in case of a kinematic model (Fig. 4c) where the backwards deflection is much less pronounced.

Further, we will show the effects of the crustal viscosity. In the previously discussed models, we used a crustal viscosity of  $10^{20}$  Pa s. Fig. 5 demonstrates the slab behaviour in three models with a low yield stress of  $10^8$  Pa. Fig. 5a is for a crustal viscosity of  $10^{19}$  Pa s, Fig. 5b for viscosity  $10^{20}$  Pa s and the last one, Fig. 5c, for a crustal viscosity of  $10^{21}$  Pa s. All of them are for a kinematic boundary condition on the subducting plate. When a low viscosity of  $10^{19}$  Pa s is considered, the weak crust is not able to transfer the prescribed surface velocity to the underlying strong plate. Consequently, the plate velocity calculated within the subcrustal strong plate is varying between 4 and 10 cm/yr reflecting the buoyancy forces of the subducted slab and phase transitions related buoyancy forces. Furthermore, the crust is now too weak and after 14 Myr evolution we observed a kind of a tearing - the subducting plate detaches from the overriding one and the subduction channel broadens significantly (Fig. 5a). The intermediate crustal viscosity of  $10^{20}$  Pa s produces a viable subduction (Fig. 5b) as already discussed above. The last value of crustal viscosity tested is  $10^{21}$  Pa s. The subduction in this model case is slow (relatively high viscosity of the crust transfers the surface boundary condition to the underlying stiff plate effectively and thus the plate velocity remains close to the prescribed value of 5 cm/yr throughout the calculation). The high crustal viscosity is however not very effective in the decoupling of the subducting and overriding plates. After 25 Myr of evolution, the subduction stops (Fig. 5c) and shortly afterwards the subducted slab detaches.



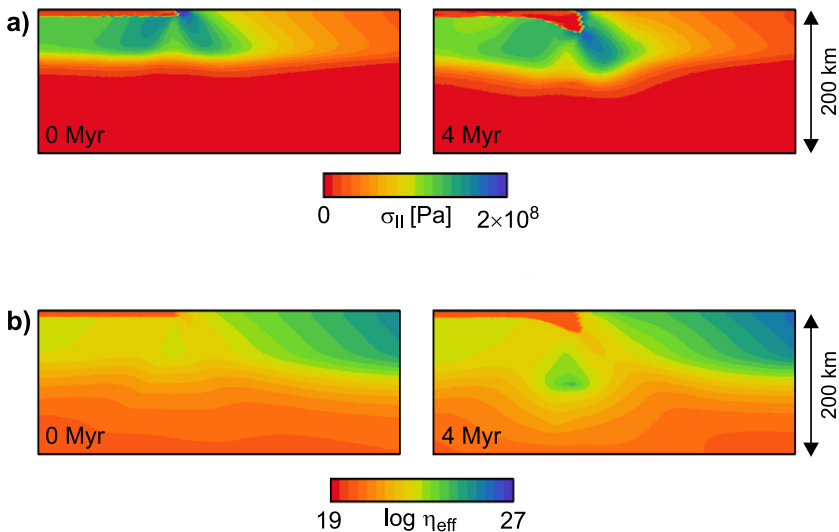
**Fig. 5.** a) Logarithm of effective viscosity in one snapshot in the model with a yield stress of 0.1 GPa and crustal viscosity of  $10^{19}$  Pa s. 2000 km wide and 2000 km deep part of the model domain is shown. White lines indicate the position of the major phase transitions at 410 km and 660 km. b) The same but for the model with crustal viscosity of  $10^{20}$  Pa s. c) The same but for the model with crustal viscosity of  $10^{21}$  Pa s.



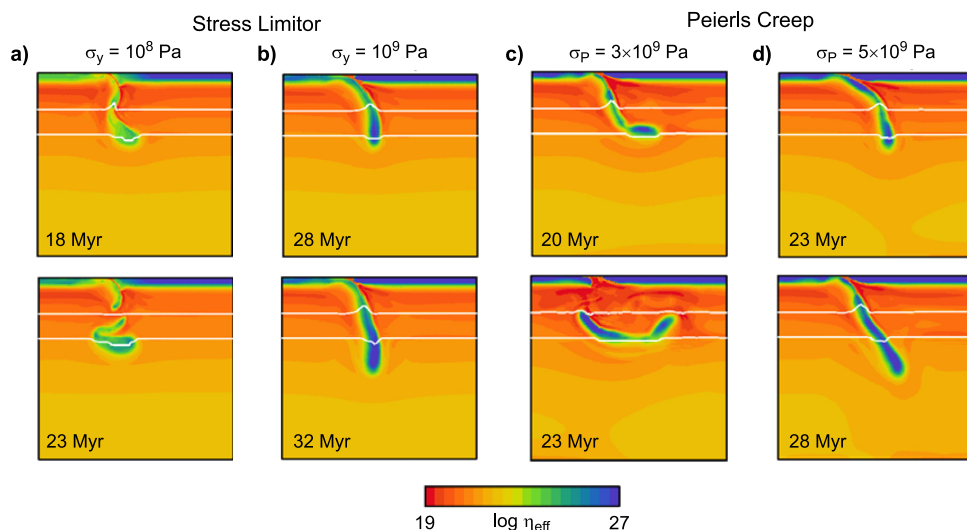
**Fig. 6.** Summary of the slab morphologies obtained in different models. Each panel shows one snapshot of the slab evolution at the time when the slab tip reaches the depth of  $\sim 1000$  km. **a)** Models with the viscosity continuously increasing with depth. **b)** Models with an additional viscosity jump by a factor of 10 at the 660 km phase interface. Logarithm of the effective viscosity in a part of the model domain 2000 km deep and 2000 km wide is shown. White lines indicate the positions of the phase boundaries at 410 km and 660 km.

Fig. 6 demonstrates the variety of the slab deformation scenarios in the upper mantle and transition zone for several models with different boundary conditions, yield stress and lower mantle viscosity. Each panel shows one snapshot of the slab evolution at about the time when the slab tip has reached the shallow lower mantle (the depth of  $\sim 1000$  km). The upper row summarises the models with the viscosity continuously increasing with depth (cf. Fig. 6a, left panel), the bottom row shows the corresponding models with an additional viscosity jump at the 660 km phase interface (Fig. 6b, left panel). All models have the same crustal viscosity of  $10^{20}$  Pa s. The models without the viscosity increase (Fig. 6a) show some general common features – the slabs subduct almost vertically and penetrate the 660 km phase boundary. The details of the slab deformation and morphology are however quite different for different parameters due to the nonlinear rheology. The differences among the models in the upper mantle and transition zone are perhaps less pronounced if the viscosity jump at 660 km is assumed. In these cases the plate velocities are significantly lower (of the order of 5–7 cm/yr) and thus the nonlinear rheological effects are less important. These models also produce a significant buckling in the upper part of the lower mantle (*Běhounková and Čížková, 2008*) that is in agreement with the tomographic results showing the blob-like rather than plate-like structures there (e.g. *van der Hilst, 1995; Bijwaard et al., 1998*).

Finally, we will show the effects of the initial geometry of the crustal layer. Above we have discussed the A type models where the geometry of the contact of the subducting and overriding plates was initially prescribed (Fig. 1b) - the weak crust initially followed a smooth arc with a radius of 800 km. We have tested the effect of the radius of curvature of this arc and we found it is negligible in the range 400–1200 km. The fact that the curved arc was actually present in the model setup was however reflected in the geometry of the subducted slab in some model cases, especially those with a high yield stress (cf. Fig. 4b). Therefore we introduced the series of B type models where the geometry of the contact was not prescribed initially (Fig. 1c). The contact zone between the subducting and overriding plates develops due to the nonlinear rheology. When pushing the subducting plate kinematically against the stagnant (no slip) overriding plate two narrow shear zones characterised by a high stress and thus (through the stress dependent rheology) low viscosity develop at the end of the subducting plate (Fig. 7). The low viscosity channel dipping under an angle of about  $60^\circ$  then enables the initiation of subduction as the weak crustal material is pushed in there. The geometry of this contact zone develops in accordance with the rheological parameters of a given model (the crustal viscosity and the yield stress). Note that all models that we will show below have a kinematic boundary condition (5 cm/yr) - the discontinuous surface velocity is necessary to produce the initial stress accumulation in the shear zones and thus provide the necessary weakening for the subduction initiation. Since in these models the resulting slab geometry is particularly sensitive to the rheological description, we will show here both the models with the stress limiter and models with Peierl's creep (Eq. (9)).



**Fig. 7.** Detail of the model domain around the trench 200 km deep and 500 km wide. **a)** Second invariant of the deviatoric stress in two time instants: 0 Myr and 4 Myr. **b)** Logarithm of the effective viscosity in the same snapshots.



**Fig. 8.** Summary of the slab morphologies in four models without prescribed weak crustal arc. Crustal viscosity is  $10^{20}$  Pa s in all models shown. Each model is represented by two snapshots illustrating the slab evolution. **a)** Model with stress limiter and the yield stress 0.1 GPa. **b)** Model with stress limiter and the yield stress 1 GPa. **c)** Model with Peierls creep and the Peierls stress 3 GPa. **d)** Model with Peierls creep and the Peierls stress 5 GPa. Logarithm of the effective viscosity in a part of the model domain 2000 km deep and 2000 km wide is shown. White lines indicate the major phase transitions at the depths of 410 km and 660 km.

The crustal viscosity in all these models is  $10^{20}$  Pa s. The results are summarised in Fig. 8. Four models are shown here: two with a stress limiter (8a and 8b) and two with Peierls creep (Figs 8c and 8d). For each model two snapshots are given demonstrating the slab evolution. First, let us compare the results with a stress limiter (Fig. 8ab) with the corresponding models with prescribed initial arc (cf. Figs 2a and 4a). The morphology of the slab with a lower yield stress of 0.1 GPa (Fig. 8a) is quite different - at the time of about 20 Myr slab detachment is observed in the transition zone that did not occur in the model with a predefined arc. Also the model with a higher yield stress of 1 GPa (Fig. 8b) differs from its corresponding model with predefined arc (Fig. 4a) - there is no backward deflection of the slab now and it penetrates vertically to the lower mantle, while some (though not very pronounced) backwards deflection occurred in the model with arc. The last two panels show the results for the models with Peierls creep with two values of the Peierls stress - 3 GPa (Fig. 8c) and 5 GPa (Fig. 8d). Peierls creep has a stronger stress dependence of viscosity, we therefore observe more weakening where the stress is locally high (e.g. the bending shallow part). That results in slab detachment in a model with  $\sigma_P$  of 3 GPa (Fig. 8c). The results with Peierls stress of 5 GPa are qualitatively very close to the case with stress limiter with a yield stress of 1 GPa. If we increase the Peierls stress  $\sigma_P$  to yet higher value of 8.5 GPa, slab is already too stiff and consequently the initial phase of the subduction process is extremely slow - it takes almost 40 Myr before the slab reaches the 410-km phase boundary. On the other hand, decreasing Peierls stress to an extremely

low value of 1 GPa produces slab that is too weak and instead of a continuous descent through the upper mantle we rather observe drops of cold material repeatedly detaching and reaching the bottom of the transition zone.

#### 4. CONCLUDING REMARKS

We have performed numerical simulations of subduction in the upper mantle and transition zone in order to estimate the sensitivity of slab deformation to various model parameters, especially shallow decoupling of the subducting and overriding plates. We have tested two groups of models: i) with a prescribed geometry of the contact between the plates (type A) and ii) models where the geometry of the contact zone develops according to the parameters of the plates (type B). In most of our studied model cases the slab arrives at the 660 km boundary under rather steep angle and penetrates to the lower mantle. Temporary stagnation of slab subduction is observed in model cases with a lower yield stress when the slab arrives at 660 km under a dip angle of about  $60^\circ$  while an unhindered penetration occurs in models with a strong slab dipping vertically or even showing the backwards deflection. This is in agreement with the conclusions of *Torii and Yoshioka (2007)*, demonstrating the effects of slab dip on its stagnation in the transition zone.

We have demonstrated that while the basic features of slab deformation - e.g. the ability to penetrate to the lower mantle - are not affected by the studied parameters, details of the slab morphology in the upper mantle and transition zone are quite sensitive to the parameterisation. First let us summarise the models with a predefined contact arc. Considering the developed slabs (i.e. at the moment when the tip already arrived at about the depth of 1000 km) we observe that the weak slabs are characterised by almost vertical shallow dip and show strong deformation around 660 km depth due to the resistance of the endothermic phase transition. The strong slabs on the other hand have a smaller shallow dip ( $50\text{--}60^\circ$ ), to certain extent keep the curvature obtained along the contact of the subducting and overriding plates and penetrate into the lower mantle without experiencing much deformation. In the B group of models the initial contact geometry is not prescribed but develops selfconsistently. Here the weak slabs (yield stress of 0.1 GPa) evolve similarly to the models with a prescribed arc. On the other hand, the morphology of the strong slabs (yield stress of 1 GPa) is different - as there is no geometry prescribed, the slab does not inherit the arc shape, no backwards deflection develops and the slab is almost vertical in the shallow lower mantle, which seems more realistic.

Further, we focused on the influence of the stress-limiting mechanism assumed in the rheological description. Except of the power-law stress limiter we also used Peierls creep and tested the effect of Peierls stress. The value of Peierls stress is not well constrained and its preferred value of 8.5 GPa may be reduced significantly (by about a factor of 2) for example due to the presence of impurities (*Kameyama, 1999*). We demonstrate here that using the Peierls creep mechanism in the rheological description instead of the power-law stress limiter affects the viscosity in the regions of the high stress accumulation - especially the bending part of the subducting plate at the contact with the overriding plates. Intermediate Peierls stress (5 GPa) produces relatively stiff slab continuously subducting and penetrating to the lower mantle. Its dip angle is somewhat lower than in

the model with power-law stress limiter (yield stress 1 GPa). Lower Peierls stress (3 GPa) allows for significant deformation at the 660-km discontinuity and later results in slab detachment. Higher Peierls stress (8.5 GPa) produces slab that is very stiff and thus extremely difficult to deform in the initial phase of subduction. On the other hand, low value of Peierls stress (1 GPa) already produces slab too weak to be able to subduct as a plate - drops of detached weak cold material sinking through the upper mantle are then observed.

Results in a model with Peierls stress of 5 GPa are rather similar to the stress-limiter case of 1 GPa. The details of the slab deformation may however differ between the Peierls creep and stress-limiter models, especially locally where high stresses accumulate. Correspondence between these two groups of models will therefore generally depend on the model setup that determines the stresses. Nevertheless, taking into account the ambiguities in Peierls creep parameters, we believe that power-law stress limiter may be accepted as a reasonable approximation of Peierls creep.

While the slab morphology is in the first place affected by the slab strength, its subduction velocity is controlled by the prescribed crustal viscosity. The free-slip runs, where the plate velocity reflects the buoyancy forces in the model, show unrealistically high plate velocities of about 40 cm/yr during the slab descent through the lower mantle for the crustal viscosity of  $10^{19}$  Pa s. With a higher viscosity of the crustal layer ( $10^{21}$  Pa s) reasonable plate velocities of the order of 5 cm/yr are obtained. However in this case the subducting plate tends to stick to the overriding one and the subduction process stops at certain moment. Yet higher crustal viscosities result in a locked slab situation and subduction process stops. Preferred value of the decoupling layer viscosity is  $10^{20}$  Pa s, only slightly higher than the viscosity of serpentinite reported by *Hilaireret et al. (2007)*. It effectively decouples the subducting and overriding plates and produces most reasonable slab morphologies (no sticking occurs in any phase of the subduction process), the plate velocities are however still rather high (of the order of 15 cm/yr). An additional viscosity jump by a factor of 10 at 660 km depth is then needed to limit the plate velocities to a reasonable values between 5–7 cm/yr. The viscosity increase is also needed to produce the slab thickening observed in seismic tomography. Vertical buckling in the transition zone and upper part of the lower mantle is observed in all models with a viscosity increase at 660-km interface as our model setup does not allow the trench rollback. Trench retreat would probably result in flat lying slabs at the base of the transition zone as observed, e.g., by *Goes et al. (2008)*.

As shown by *Quinteros et al. (2010)*, slab velocity is also very sensitive to the viscosity of the transition zone – their preferred value lies between  $3 \times 10^{20}$ – $10^{21}$ . Our transition zone viscosity is between  $5 \times 10^{20}$ – $10^{21}$  Pa s. In order to obtain a viable model of continuous subduction both the weak crust and stress-limiting slab rheology are needed. A yield strength of the order of about 0.1–1 GPa ensures that the slab may be able to bend and subduct continuously. Higher yield stress results in slabs too stiff to bend while the yield stresses at the lower end of the above mentioned range result in breakoff and ceasing of the subduction process. The presence of the weak crust is also crucial - without its lubricating effect the locked slab situation results.

All models presented here have a fixed surface with either a free-slip or kinematic surface boundary conditions at the top of the subducting plate. Thus the free surface deformation that may be an important ingredient affecting the shallow slab behavior (e.g. Gurnis et al., 1996; Kaus et al., 2010; Cramer et al., 2012) is not possible here. However, as shown by Quinquis et al. (2011) and Chertova et al. (2012), its effect could be to a large extent compensated by the presence of a weak crustal layer. We thus believe that our results should not be significantly biased by this model assumption.

Our results demonstrate that slab evolution and deformation in the upper mantle and the transition zone is quite sensitive not only to the rheological parameters of the mantle, but also to the decoupling mechanism at the contact of the subducting and overriding plates. Due to the strongly stress dependent rheology of slabs, the friction on the contact between the subducting and overriding plates controlled by the crustal viscosity affects also the viscosity within the slab. The effects of both the slab rheology and the approximation of the plates decoupling should thus be always cautiously evaluated.

*Acknowledgements:* We thank Javier Quinteros, Scott King and Sergio Zlotnik for comments that helped to improve the manuscript and Ctirad Matyska and Ondřej Čadek for inspiring discussions. This research has been supported by the Czech Science Foundation Grant P210/11/1366, by the research project MSM0021620860 of the Czech Ministry of Education and the Netherlands Research School for Integrated Solid Earth Science (ISES).

#### References

- Auth Ch., Bercovici D. and Christensen U.R., 2003. Two-dimensional convection with a self-lubricating, simple-damage rheology. *Geophys. J. Int.*, **154**, 783–800.
- Balachandar S., Yuen D.A. and Reuteler D., 1995a. Localization of toroidal motion and shear heating in 3-D high Rayleigh number convection with temperature dependent viscosity. *Geophys. Res. Lett.*, **22**, 477–480.
- Balachandar S., Yuen D.A., Reuteler D.M. and Lauer G.S., 1995b. Viscous dissipation in 3-dimensional convection with temperature-dependent viscosity. *Science*, **267**, 1150–1153.
- Běhouňková M. and Čížková H., 2008. Long-wavelength character of subducted slabs in the lower mantle. *Earth Planet. Sci. Lett.*, **275**, 43–53.
- Bercovici D., 1996. Plate generation in a simple model of lithosphere-mantle flow with dynamic self-lubrication. *Earth Planet. Sci. Lett.*, **144**, 41–51.
- Bercovici D., 1998. Generation of plate tectonics from lithosphere-mantle flow and void-volatile self-lubrication. *Earth Planet. Sci. Lett.*, **154**, 139–151.
- Bercovici D., Ricard Y. and Richards M., 2000. The relation between mantle dynamics and plate tectonics: A primer. In: Richards M.A., Gordon R. and van der Hilst R. (Eds.), *History and Dynamics of Global Plate Motions. Geophysical Monograph Series*, **121**, American Geophysical Union, Washington, D.C., 5–46.
- Bercovici D., Ricard Y. and Schubert G., 2001. A two-phase model of compaction and damage, 3. Applications to shear localization and plate boundary formation. *J. Geophys. Res.*, **106**, 8925–8940.

- Bercovici D., 2003. The generation of plate tectonics from mantle convection. *Earth Planet. Sci. Lett.*, **205**, 107–121.
- Bercovici D. and Ricard Y., 2003. Energetics of a two phase model of lithospheric damage, shear localization and plate boundary formation. *Geophys. J. Int.*, **152**, 1–16.
- Bijwaard H., Spakman W. and Engdahl E.R., 1998. Closing the gap between regional and global travel time tomography. *J. Geophys. Res.*, **103**, 30055–30075.
- Billen M.I., 2010. Slab dynamics in the transition zone. *Phys. Earth Planet. Inter.*, **183**, 296–308.
- Billen M.I., Gurnis M. and Simons M., 2003. Multiscale dynamic models of the Tonga-Kermadec subduction zone. *Geophys. J. Int.*, **153**, 359–388.
- Billen M.I. and Hirth G., 2005. Newtonian versus non-Newtonian upper mantle viscosity: Implications for subduction initiation. *Geophys. Res. Lett.*, **32**, L19304, DOI: 10.1029/2005GL023457.
- Billen M. and Hirth G., 2007. Rheologic controls on slab dynamics. *Geochem. Geophys. Geosyst.*, **8**, DOI: 10.1029/2007GC001597.
- Bina C. and Helffrich G., 1994. Phase transition Clapeyron slopes and transition zone seismic discontinuity topography. *J. Geophys. Res.*, **103**, 15853–15860.
- Chertova M., Geenen T., van den Berg A.P. and Spakman W., 2012. Using open sidewalls for modelling self-consistent lithosphere subduction dynamics. *Solid Earth Discuss.*, **4**, 707–744.
- Čížková H., van Hunen J., van den Berg A. P. and Vlaar N.J., 2002. The influence of rheological weakening and yield stress on the interaction of slabs with the 670-km discontinuity. *Earth Planet. Sci. Lett.*, **199**, 447–457.
- Čížková H., van Hunen J. and van den Berg A.P., 2007. Stress distribution within subducting slabs and their deformation in the transition zone. *Phys. Earth Planet Inter.*, **161**, 202–214.
- Cramer F., Tackley P.J., Meilick I., Gerya T. and Kaus B.J.P., 2012. A free plate surface and weak oceanic crust produce single-sided subduction on Earth. *Geophys. Res. Lett.*, DOI: 10.1029/2011GL050046.
- Duretz T., Gerya T.V. and May D.A., 2011. Numerical modelling of spontaneous slab breakoff and subsequent topographic response. *Tectonophysics*, **502**, 244–256.
- Gerya T., Connolly J.A.D. and Yuen D.A., 2008. Why is terrestrial subduction one-sided? *Geology*, **36**, 43–46.
- Gerya T.V. and Meilick F.I., 2011. Geodynamic regimes of subduction under an active margin: effects of rheological weakening by fluids and melts. *J. Metamorph. Geol.*, **29**, 7–31, DOI: 10.1111/j.1525-1314.2010.00904.x.
- Goes S., Capitanio F.A. and Morra G., 2008. Evidence of lower-mantle slab penetration phases in plate motions. *Nature*, **451**, 981–984.
- Gurnis M., Eloy C. and Zhong S., 1996. Free-surface formulation of mantle convection ii. implication for subduction-zone observables. *Geophys. J. Int.*, **127**, 719–727.
- Gurnis M. and Hager B., 1988. Controls on the structure of subducted slabs. *Nature*, **335**, 317–321.
- Han L. and Gurnis M., 1999. How valid are dynamic models of subduction and convection when plate motions are prescribed? *Phys. Earth Planet. Inter.*, **110**, 235–246.

- Hilairt N., Reynard B., Wang Y., Daniel I., Merkel S., Nishiyama N. and Petitgirard S., 2007. High-pressure creep of serpentine, interseismic deformation, and initiation of subduction. *Science*, **318**, 1910–1913.
- Hirth G. and Kohlstedt D., 2003. Rheology of the upper mantle and mantle wedge: a view from the experimentalists. In: Eiler J. (Ed.), *Inside the Subduction Factory. Geophysical Monograph Series*, **138**. American Geophysical Union, Washington, D.C., 83–105.
- Ita J. and King S.D., 1994. Sensitivity of convection with an endothermic phase change to the form of governing equations, initial conditions, boundary conditions, and equation of state. *J. Geophys. Res.*, **99**, 15919–15938.
- Jacobs M.H.G. and van den Berg A.P., 2011. Complex phase distribution and seismic velocity structure of the transition zone: convection model predictions for a magnesium-endmember olivine-pyroxene mantle. *Phys. Earth Planet. Inter.*, **186**, 36–48.
- Jadamec M. and Billen M.I., 2010. Reconciling rapid 3-D mantle flow and surface plate motions near the Eastern Alaska slab edge. *Nature*, **465**, 338–341.
- Kameyama M., Yuen D.A. and Karato S.-i., 1999. Thermal-mechanical effects of low-temperature plasticity (the Peierls mechanism) on the deformation of a viscoelastic shear zone. *Earth Planet. Sci. Lett.*, **168**, 159–172.
- Karato S.I. and Wu P., 1993. Rheology of the upper mantle: a synthesis. *Science*, **260**, 771–778.
- Kaus B.J.P., Mühlhaus H.-B. and May D.A., 2010. A stabilization algorithm for geodynamic numerical simulations with a free surface. *Phys. Earth Planet. Inter.*, **181**, 12–20.
- Kincaid C. and Sacks I.S., 1997. Thermal and dynamical evolution of the upper mantle in subduction zones. *J. Geophys. Res.*, **102(B6)**, 12295–12315.
- King S.D. and Hager B.H., 1990. The relationship between plate velocity and trench viscosity in Newtonian and power-law subduction calculations. *Geophys. Res. Lett.*, **17**, 2409–2412.
- King S. and Hager B., 1994. Subducted slabs and the geoid 1. Numerical experiments with temperature-dependent viscosity. *J. Geophys. Res.*, **99(B10)**, 19843–19852.
- Kukačka M. and Matyska C., 2004. Influence of the zone of weakness on dip angle and shear heating of subducted slab. *Phys. Earth Planet. Inter.*, **141**, 243–252.
- Larsen T., Yuen D.A. and Malevsky A.V., 1995. Dynamical consequences of fast subducting slabs from a self-regulating mechanism due to viscous heating in variable viscosity convection. *Geophys. Res. Lett.*, **22**, 1277–1280.
- Larsen T., Yuen D.A., Smedso J.L. and Malevsky A.V., 1996. Thermomechanical modeling of pulsation tectonics and consequences on lithospheric dynamics. *Geophys. Res. Lett.*, **23**, 217–220.
- Lee Ch. and King S., 2011. Dynamic buckling of subducting slabs reconciles geological and geophysical observations. *Earth Planet. Sci. Lett.*, **312**, 360–370.
- McNamara K., Karato S.I. and van Keken E., 2001. Localization of dislocation creep in the lower mantle: implications for the origin of seismic anisotropy. *Earth Planet. Sci. Lett.*, **191**, 85–99.
- Maierová P., Chust T., Steinle-Neumann G., Čadek O. and Čížková H., 2012. The effect of a realistic thermal diffusivity on numerical model of a subducting slab. *J. Geophys. Res.*, **117**, B07202, DOI: 10.1029/2011JB009119.

- Moresi L. and Solomatov S., 1998. Mantle convection with a brittle lithosphere: Thoughts on the global tectonic style of the Earth and Venus. *Geophys. J.*, **133**, 669–682.
- Quinquis M., Buitter S. and Ellis S., 2011. The role of boundary conditions in numerical models of subduction zone dynamics. *Tectonophysics*, **497**, 57–70.
- Quinteros J., Sobolev S.V. and Popov A.A., 2010. Viscosity in transition zone and lower mantle: Implications for slab penetration. *Geophys. Res. Lett.*, **37**, DOI: 10.1029/2010GL043140.
- Quinteros J. and Sobolev S., 2012. Constraining kinetics of metastable olivine in the Marianas slab from seismic observations and dynamic models. *Tectonophysics*, 526–529, 48–55.
- Regeneuer-Lieb K. and Yuen D.A., 2003. Modeling shear zones in geological and planetary sciences: solid- and fluid- thermal-mechanical approaches. *Earth. Sci. Rev.*, **63**, 295–349.
- Ricard Y. and Bercovici D., 2003. Two-phase damage theory and crustal rock failure: the theoretical 'void' limit and the prediction of experimental data. *Geophys. J. Int.*, **155**, 1057–1064.
- Richards M., Yang W.-S., Baumgardner J. and Bunge H.P., 2001. Role of a low-viscosity zone in stabilizing plate tectonics: Implications for comparative terrestrial planetology. *Geochem. Geophys. Geosyst.*, 2000GC000115.
- Rolf T. and Tackley P.J., 2011. Focussing of stress by continents in 3D spherical mantle convection with self-consistent plate tectonics. *Geophys. Res. Lett.*, **38**, L18301, DOI: 10.1029/2011GL048677
- Schmeling H., 1989. Compressible convection with constant and variable viscosity: The effect on slab formation geoid and topography. *J. Geophys. Res.*, **94**, 12463–12481.
- Segal A. and Praagman N. P., 2005. *The Sepran FEM Package*. Technical Report. Ingenieurs-Bureau Sepra, The Netherlands (<http://ta.twi.tudelft.nl/sepran/sepran.html>).
- Sizova E., Gerya T., Brown M. and Perchuk L.L., 2010. Subduction styles in the Precambrian: Insight from numerical experiments. *Lithos*, **116**, 209–229, DOI:10.1016/j.lithos.2009.05.028.
- Sobolev S.V. and Babeyko A.Y., 2005. What drives orogeny in the Andes? *Geology*, **33**, 617–620.
- Stein C., Schmalz J. and Hansen U., 2004. The effect of rheological parameters on plate behaviour in a self-consistent model of mantle convection. *Phys. Earth Planet. Inter.*, **142**, 225–255.
- Stein C. and Hansen U., 2008. Plate motions and the viscosity structure of the mantle-insights from numerical modelling. *Earth Planet. Sci. Lett.*, **272**, 29–40.
- Steinbach V. and Yuen D.A., 1995. The effects of temperature dependent viscosity on mantle convection with two mantle major phase transitions. *Phys. Earth Planet. Inter.*, **90**, 13–36.
- Tackley P.J., 1998. Self-consistent generation of tectonic plates in three-dimensional mantle convection. *Earth Planet. Sci. Lett.*, **157**, 9–22.
- Tackley P.J., 2000a. Self-consistent generation of tectonic plates in time-dependent, three-dimensional mantle convection simulations, 1. pseudoplastic yielding. *Geochem. Geophys. Geosyst.*, **1**, 2000GC000,036.
- Tackley P.J., 2000b. Self-consistent generation of tectonic plates in time-dependent, three-dimensional mantle convection simulations, 2. strain weakening and asthenosphere. *Geochem. Geophys. Geosyst.*, **1**, 2000GC000,043.

- Tackley P.J., 2000c. The quest for self-consistent generation of plate tectonics in mantle convection models. In: Richards M.A., Gordon R. and van der Hilst R. (Eds.), *History and Dynamics of Global Plate Motions. Geophysical Monograph Series*, **121**. American Geophysical Union, Washington, D.C., 47–72.
- Tackley P.J., 2000d. Mantle convection and plate tectonics: Toward an integrated physical and chemical theory. *Science*, **288**, 2002–2007.
- Torii Y. and Yoshioka S., 2007. Physical conditions producing slab stagnation: Constraints of the Clapeyron slope, mantle viscosity, trench retreat, and dip angles. *Tectonophysics*, **445**, 200–209.
- Trompert R. and Hansen U., 1998. Mantle convection simulations with rheologies that generate plate-like behaviour. *Nature*, **395**, 686–689.
- van Avendonk H., Holbrook W.S., Lizarralde D., Mora M.M., Harder S., Bullock A.D., Alvarado G.E. and Ramrez C.J., 2010. Seismic evidence for fluids in fault zones on top of the subducting Cocos Plate beneath Costa Rica. *Geophys. J. Int.*, **181**, 997–1016, DOI: 10.1111/j.1365-246X.2010.04552.x.
- van Avendonk H., Holbrook W.S., Lizarralde D. and Denyer P., 2011. Structure and serpentinization of the subducting Cocos plate offshore Nicaragua and Costa Rica. *Geochem. Geophys. Geosyst.*, **12**, DOI: 10.1029/2011gc003592.
- van den Berg A.P., Yuen D.A. and van Keken P.E., 1991. Effects of depth-variations in creep laws on the formation of plates in mantle dynamics. *Geophys. Res. Lett.*, **18**, 2197–2200.
- van den Berg A.P., van Keken P.E., and Yuen D.A., 1993. The effects of a composite non-Newtonian and Newtonian rheology on mantle convection. *Geophys. J. Int.*, **115**, 62–78.
- van der Hilst R., 1995. Complex morphology of subducted lithosphere in the mantle beneath the Tonga trench. *Nature*, **374**, 154–157.
- van der Meer D.G., Spakman W., van Hinsbergen D.J.J., Amaru M.L. and Torsvik T.H., 2010. Towards absolute plate motions constrained by lower-mantle slab remnants. *Nature Geosci.*, **3**, 36–40.
- van Heck H. and Tackley P.J., 2008. Plate tectonics on super-Earths: Equally or more likely than on Earth. *Earth Planet. Sci. Lett.*, **310**, 252–261.
- van Hunen J., van den Berg A.P. and Vlaar N.J., 2000. A thermo-mechanical model of horizontal subduction below an overriding plate. *Earth Planet. Sci. Lett.*, **182**, 157–169.
- van Hunen J., van den Berg A.P. and Vlaar N.J., 2001. Latent heat effects of the major mantle phase transitions on low-angle subduction. *Earth Planet. Sci. Lett.*, **190**, 125–135.
- van Hunen J., van den Berg A.P. and Vlaar N.J., 2002. On the role of subducting oceanic plateaus in the development of shallow flat subduction. *Tectonophysics*, **352**, 317–333.
- van Hunen J., van den Berg A.P. and Vlaar N.J. 2004. Various mechanisms to induce present-day shallow flat subduction and implications for the younger Earth: a numerical parameter study. *Phys. Earth Planet. Inter.*, **146**, 179–194.
- van Hunen J. and Allen M.B., 2011. Continental collision and slab break-off: A comparison of 3-D numerical models with observations. *Earth Planet. Sci. Lett.*, **302**, 27–37.
- Yamazaki D., Karato S., 2001. Some mineral physics constraints on rheology and geothermal structure of earth's lower mantle. *Am. Mineral.*, **86**, 358–391.

*Rheological decoupling and slab deformation*

- Zhong S. and Gurnis M., 1986. Interaction of weak faults and non-Newtonian rheology produces plate tectonics in a 3-D model of mantle flow. *Nature*, **383**, 245–247.
- Zhong S. and Gurnis M., 1995a. Mantle convection with plates and mobile, faulted plate margins. *Science*, **267**, 838–843.
- Zhong S. and Gurnis M., 1995b. Towards a realistic simulation of plate margins in mantle convection. *Geophys. Res. Lett.*, **22**, 981–984.
- Zhong S., Gurnis M. and Moresi L., 1998. Role of faults, nonlinear rheology, and viscosity structure in generating plates from instantaneous mantle flow models. *J. Geophys. Res.*, **103(B8)**, 15255–15268.